Chapter 7
Do We Need Clinical Applications in Synchrotrons?

Check for updates

In general, the use of synchrotron radiation provides ideal working conditions for X-ray imaging which derive from the high flux, spatial and temporal coherence of the beam. On the other side, synchrotron light sources are huge facilities, limited in number, with high operational costs and infrastructural requirements. In other words, it can be questioned whether it is worth using a synchrotron facility for a given clinical imaging application or not. The answer to this question lies in the comparison between results obtained with SR and with more 'conventional' systems available in clinical or laboratory environments. In this context, the aim of the present chapter is to investigate the performances of two conventional systems with rather different application fields. In the next section, a first of its kind phantom-based comparison study between a clinically available BCT system and the SR PB imaging setup will be presented. In the second section the performances and possible applications of a state-of-the-art rotating-anode micro-CT system, capable of providing spatial and temporal coherence, are investigated. The last section will try to answer to the rather complex question kicking-off this chapter and it will provide a general overview of many existing or soon-to-come clinical applications of synchrotrons.

7.1 Synchrotron and Clinical BCT: A Comparison Study

In this section a direct quantitative and qualitative comparison between tomographic images of a breast-like phantom acquired by using both the SR setup and a clinical BCT machine in use at the Radboud University Medical Center (Nijmegen, The Netherlands) is presented, based on the results published in [1].

As discussed in Sect. 3.1, progresses in the development of BCT have been made in recent years and an increasing number of dedicated BCT systems with different acquisition modes (e.g., cone-beam, parallel-beam, helical) and detector types (e.g., flat-panels, photon-counting) have been proposed. In this lively context, there

is still a lack of image quality comparisons and no quantitative study performed among different systems, either based on conventional or synchrotron sources, has been published to date. Of course a higher image quality from synchrotron data is expected, but assessing the difference with clinically available systems can provide a benchmark on the current level of behaviour of SR-based techniques, and therefore establish its potential for clinical implementation. In other words, only showing that the gap with conventional techniques is substantial can provide justification for a SR clinical application.

This study makes use of both quantitative (objective) and qualitative (subjective) criteria. Specifically, signal-to-noise ratio (SNR), contrast-to-noise ratio (CNR), spatial resolution and noise power spectrum (NPS) are hereby used as indicators of image quality, possibly determining its diagnostic effectiveness. Namely, as discussed in previous chapters, SNR and CNR are related to low-contrast detail visibility (e.g., glandular tissue embedded in an adipose background), the shape of NPS reveals the image texture (i.e. low-frequency-peaked NPS are related to coarse image graininess; high-frequency-peaked NPS results in a finer grain noise) and spatial resolution determines the ability to detect small (high-contrast) details such as microcalcifications [2]. The comparison makes use of a breast-like phantom containing inserts mimicking relevant diagnostic features. The exposure parameters were automatically determined by the clinical BCT, while the SR irradiation parameters were tuned to replicate, as close as possible, the clinical conditions in terms of X-ray energy and delivered radiation dose.

7.1.1   BCT Dedicated Phantom and Experimental Setup

The used dedicated BCT phantom is shown in Fig. 7.1. It is produced by CIRS (model #12-685) and it has a semi-ellipsoidal truncated shape consisting of several slabs made of 100% breast-adipose equivalent material. A variety of targets are embedded into slab 9 as showed in panel (c): spheroidal masses of different diameters (1.80, 3.18, 4.76 and 6.32 mm) made of epoxy resin equivalent to breast carcinoma; cylindrical fibers of different diameters (0.15, 0.23, 0.41 and 0.60 mm); calcification clusters ($CaCO_3$) of different grain sizes (0.13, 0.20, 0.29, 0.40 mm). The phantom was positioned at the system's isocenter both for the clinical and SR BCT setups.

The considered BCT clinical system is produced by Koning (Koning Corp., West Henrietta, NY) and it is installed at Radboud University Medical Center (Nijmegen, the Netherlands) [3]. A detailed description of the system can be found in literature [4–7], while only the most relevant features to this study are hereby reported. The system has a source-to-detector distance of 92.3 cm and a source-to-isocenter distance of 65.0 cm. The X-ray source is a rotating anode featuring a nominal focal spot size of 0.3 mm, whereas tomographic projections are acquired in half-cone beam geometry. The anode is made of tungsten while aluminum filtration is used to shape the energy spectrum. The tube is operated at a fixed voltage of 49 kV(peak), corresponding to a first half value layer of 1.39 mm Al (i.e. effective X-ray energy of
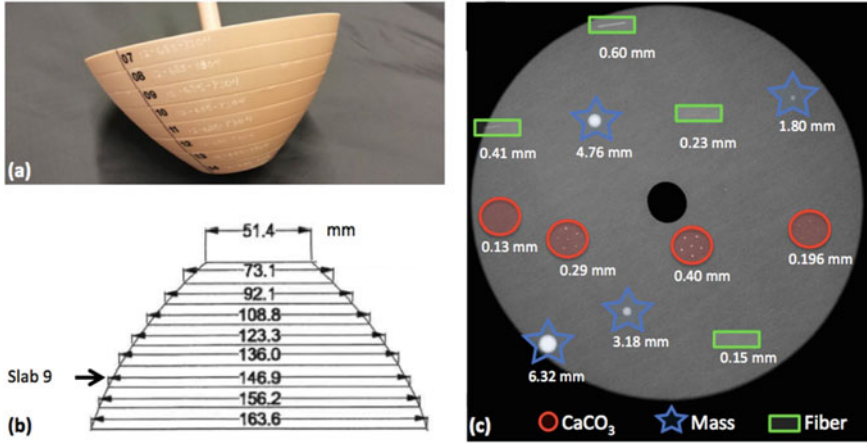
Fig. 7.1 Photograph of the phantom (**a**) and phantom dimensions in mm (**b**) (in mm). Details embedded in slab 9 (**c**): calcifications (CaCO3) in red circles, masses in blue stars and fibers in green rectangles

30.3 keV, evaluated from air kerma measurements after attenuation by various thickness of Al and using the weighted-energy average of a photon spectrum model as described in [8]). The X-ray source operates in pulse mode, with a constant 8 ms pulse length. A complete BCT acquisition consists of 300 projections over a full 360° revolution of the X-ray tube and detector in 10 s. The appropriate tube current is selected by acquiring two low-dose projections (16 mA, 2 pulses of 8 ms each per projection) images at right angles. The detector is a 39.7 cm × 29.8 8 cm flat-panel (4030CB, Varian Medical System, Palo Alto, California, USA) with a nominal pixel size of 194 μm. Tomographic reconstructions are performed according to the standard clinical workflow by using a Feldkamp-Davis-Kress (FDK)-based algorithm with a modified Shepp-Logan reconstruction filter, and an isotropic cubic voxel of $273 \times 273 \times 273 \ \mu m^3$. The main components of the system are shown in panel (a) of Fig. 7.2a while panel (b) shows the phantom positioning. The automatically selected exposure parameters determine an air kerma of 13.5 mGy, corresponding to a mean glandular dose (MGD) value of 6.5 mGy.

The synchrotron-based images were acquired following the workflow described in Chap. 3: in order to match the clinical system conditions the energy was selected to be 30 keV, while 1200 projections were acquired in a 180° rotation delivering an air kerma of 14.2 mGy, corresponding to 6.7 mGy MGD. Prior to tomographic reconstruction, projection images are phase retrieved both with single- and two-materials approaches: as discussed in Sect. 2.5 the difference lies in the input δ/β values. Specifically, in case of single-material PhR $\delta/\beta = 2267$, corresponding to breast equivalent tissue is selected, whereas for the two-materials PhR $(\delta_1 - \delta_2)/(\beta_1 - \beta_2) = 795$ corresponding to a glandular/adipose interface is chosen.
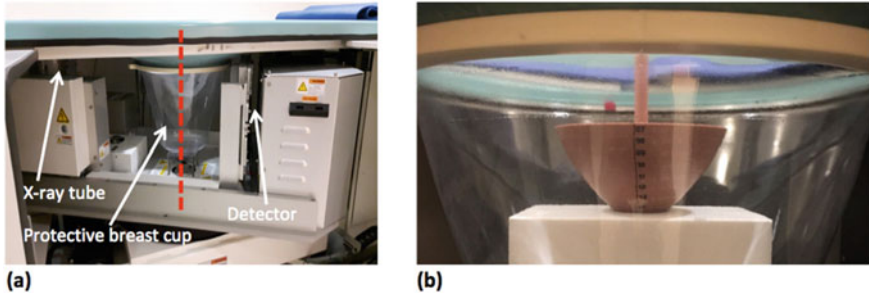
Fig. 7.2 Photograph of the main breast CT system components (**a**). The red dotted line represents the system's rotation axis (i.e. isocenter). Isocenter position of the phantom during the measurements (**b**)

Since larger δ/β values correspond to smoother PhR filter kernels, the single- and two-materials approaches are hereinafter defined as smooth and sharp PhR kernels, respectively.

7.1.2 Image Quality Analysis

The CNR has already been defined in Eq. (5.20). Of note, the use of the standard deviation of the background to represent the magnitude of image noise, implies that the noise is assumed to be ergodic. With reference to the previous definition, CNR does not capture the dependence of detail visibility on the detail's size (i.e. Rose criterion). For this reason, the 'Rose' signal-to-noise-ratio (SNR_{Rose}) metric is introduced as [9, 10]:

$$SNR_{Rose} = CNR \times \sqrt{N_{pixel}} \qquad (7.1)$$

where N_{pixel} is the number of pixel of the selected region of interest (ROI) within a given detail. Of note, this definition of signal-to-noise ratio has not to be confused with the SNR definition given in Chap. 5. Both CNR and SNR_{Rose} were evaluated for all the spheroidal masses shown in panel (c) of Fig. 7.1. As shown in panel (a) of Fig. 7.3, for each mass a circular ROI with a diameter scaling with the mass dimension was selected within the detail, while, for the background estimation, 10 evenly spaced ROIs were selected in the neighboring region. In the case of synchrotron-based datasets this analysis was repeated also by averaging 5 consecutive slices in order to match (as close as possible) the slice thickness of the clinical system, resulting in an effective voxel size of $57 \times 57 \times 250\ \mu m^3$. With this choice a similar volume of a given detail is considered in each transverse slice for both systems.

While both CNR and SNR_{Rose} depend on the magnitude of the background noise, the image texture (or graininess) is characterized by the noise power spectrum (NPS), which is the noise spectral decomposition in the Fourier space. The in-slice NPS is
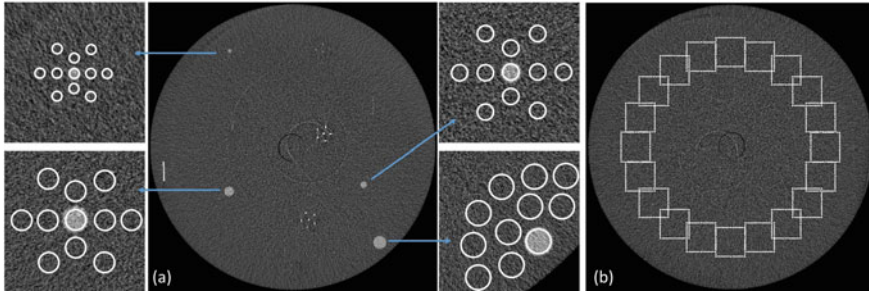
Fig. 7.3 SR-based tomographic reconstruction showing ROIs position for the CNR and SNR_{Rose} (**a**); ROIs position for the NPS evaluation in a homogeneous background are shown in (**b**)

a bi-dimensional map in Fourier space measured from a homogeneous phantom CT image by selecting equally sized ROIs and using the following definition [11, 12]:

$$\text{NPS}(u, v) = \frac{d_x d_y}{N_x N_y} \frac{1}{N_{\text{ROI}}} \sum_{i=1}^{N_{\text{ROI}}} |\mathscr{F}[I_i(x, y) - P_i(x, y)]|^2 \qquad (7.2)$$

where u, v are the spatial frequencies, d_x, d_y refers to the voxel size (in mm) along x and y dimension, N_x, N_y are the corresponding ROI dimensions measured in number of pixels, N_{ROI} is the number of selected ROIs, $\mathscr{F}$ denotes the bi-dimensional Fourier transform, $I_i(x, y)$ is the pixel value at position (x, y) of the ith ROI and $P_i(x, y)$ is a second order polynomial fit of $I_i(x, y)$. The subtraction with the polynomial term is a practical implementation of the de-trending procedure, aiming at removing any slowly-varying nonuniformities that may be caused from beam hardening effects, scattered radiation or nonuniform detector gain [12, 13]. As NPS is a spectral decomposition of image noise (σ), we have

$$\sigma^2 = \iint \text{NPS}(u, v) \, \mathrm{d}u \, \mathrm{d}v \qquad (7.3)$$

Following the procedure described by [12], in order to compare noise textures of images with different noise magnitude, the normalized NPS (nNPS) is defined as:

$$\text{nNPS}(u, v) = \frac{\text{NPS}(u, v)}{\sigma^2} \qquad (7.4)$$

In addition, since NPS maps of tomographic reconstructions usually show circular symmetry, it is common to show mono-dimensional radially averaged NPS curves making use of the identity $q = \sqrt{u^2 + v^2}$. The nNPS distributions, both bi- and mono-dimensional, were evaluated for both systems by selecting 20 evenly spaced square ROIs at a constant distance from the phantom center as shown in panel (b) of Fig. 7.3. Given the difference in the reconstructed voxel size between the two

systems, the used ROIs have a 64 × 64 pixels area for the clinical and system 256
× 256 pixels area for the synchrotron datasets, meaning that each ROI represents
a similar physical area for both systems. The uncertainty on radial nNPS curves
was assessed by repeating the measure in 10 consecutive homogeneous slices and
associating, for each spatial frequency, the corresponding standard deviation [13].

The spatial resolution of both systems was estimated directly from the images of
the homogeneous portion of the phantom by using a novel approach recently intro-
duced by Mitzutani and colleagues [14], which is based on a logarithmic intensity
plot in the Fourier domain, and it has shown consistent results for both planar and
tomographic applications [15]. The main advantage of this technique is that it allows
to estimate spatial resolution directly from general sample images, not requiring ded-
icated phantoms, under the hypothesis of a Gaussian system point spread function
(PSF). Although modern digital detectors, especially direct conversion devices, in
general do not feature Gaussian response functions, the whole imaging chain PSF
contains also the contribution of each processing step leading to the final tomo-
graphic image as detailed in Sect. 5.1.1.2. In particular, both the interpolation and
apodization filter inherent to tomographic reconstruction contribute to smoothen the
system PSF [16], usually described by a bell-shaped curve which, in case of the pre-
sented technique, is approximated by a Gaussian function. Under this assumption,
the FWHM of the PSF can be determined from

$$\ln |\mathscr{F}_r [I(x, y)]| \simeq -\frac{\pi^2}{2 \ln 2} \text{FWHM}^2 |q|^2 + \text{constant} \qquad (7.5)$$

where $\mathscr{F}_r$ is the radial Fourier transform. By performing a linear regression of the
quantity $\ln |\mathscr{F}_r [I(x, y)]|$ as a function of $|q|^2$, yielding a correlation coefficient m,
the FWHM can be easily estimated to be:

$$\text{FWHM} = \frac{\sqrt{-2 \ln 2 \times m}}{\pi} \qquad (7.6)$$

Once the FWHM of the Gaussian PSF is known, the spatial resolution corresponding
to the 10% of the modulation transfer function (MTF), measured in line-pairs per
millimeter (lp/mm), can be easily estimated from [17]:

$$\text{MTF}_{10\%}(lp/\text{mm}) = \frac{1}{1.24 \times \text{FWHM(mm)}} \qquad (7.7)$$

where the presence of the factor 1.24 is justified in the Appendix C. It should be
remarked that, since not all the PSFs can be accurately approximated by a Gaussian
function, this method cannot fully replace the direct PSF and MTF measurements
based on line-patterns or small high-absorbing details, but has to be regarded as a
fast and easy way to provide a spatial resolution estimate, possibly constituting a
method for routine checks.
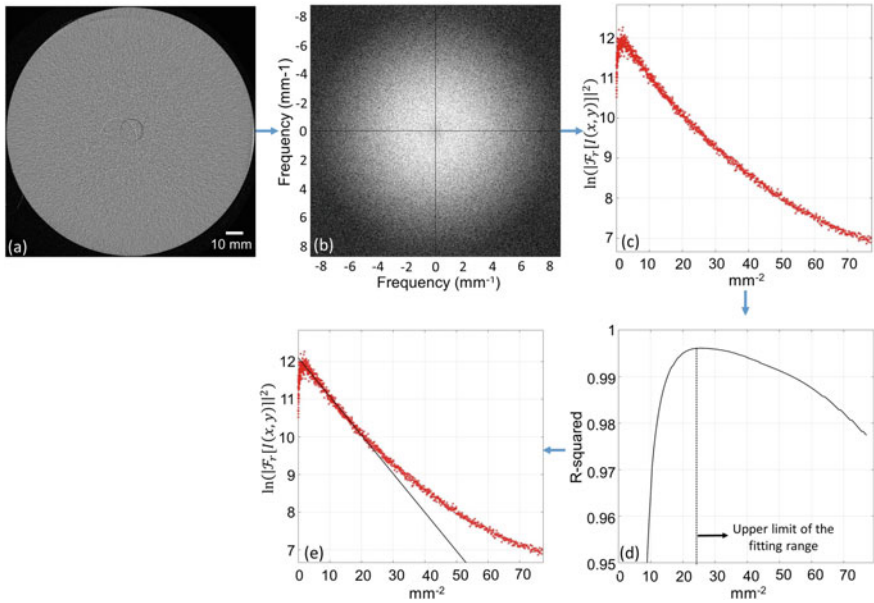
Fig. 7.4 Sketch of the implemented workflow for the estimation of spatial resolution. A detailed description of all the steps (**a**)–(**e**) can be found in text

As mentioned, this technique is rather new and not well established, so it is worth to report some practical details on its implementation. The scheme in Fig. 7.4 shows the implemented workflow for estimating the spatial resolution. A ROI comprised within an homogeneous portion of the phantom is selected (a) and the logarithm of the square modulus of its Fourier transform is computed (b). Then its radial average is plotted as a function of the spatial frequency squared (c). This plot should be fitted, in the region towards low spatial frequencies (squared), with a straight line [14, 15]. In order to identify the best fitting region, the fit procedure is repeated by finely varying the upper limit of the fitting interval and by plotting, as a function of the spatial frequency, its R-squared value (d). At this point, the fitting range yielding the maximum R-squared value is selected and the linear regression is plotted over the experimental data (e). In order to associate an uncertainty to the spatial resolution, the same procedure is repeated in 4 non-overlapping ROIs and the error is defined as the maximum difference among the spatial resolution estimates. Of note is that this procedure has been found to be robust, and compatible results are found by selecting different ROIs and/or different reconstructed slices. Moreover, it should be remarked that the PSF width is proportional to the square root of the regression coefficient, so that small inaccuracies in the fitting procedure translate in even smaller inaccuracies in the spatial resolution estimate (e.g.., a 10% error in the estimate of the regression coefficient corresponds to an error in the spatial resolution estimate of about 5%).

To complete the study of the two BCT setups, a qualitative analysis on the visibility of high-resolution details (i.e. calcification clusters and fibers) was performed by visually comparing the tomographic reconstructions of both systems.

7.1.3   BCT Image Quality Comparison: Experimental Results

Panel (a) of Figure 7.5 shows the CNR values as a function of the mass dimension for the two BCT systems (red color for the clinical and blue color for the SR system). In the case of SR images, the two phase-retrieval kernels and the two slice approaches (i.e. single slice and average over 5 consecutive slices to match the clinical slice thickness) are presented. The CNR in the clinical BCT system is higher than the SR case, regardless of the reconstruction and/or averaging methods: this is mainly due to the difference in the reconstructed voxel size. On the contrary, considering the detail visibility (i.e. the SNR_{Rose} metrics reported in panel (b)) which accounts for the number of pixels enclosed within the detail of interest, the synchrotron data show superior performances in all configurations, yielding, in case of the smooth PhR kernel and slice averaging, a 2.5–3 times higher SNR_{Rose} for all mass diameters.

Panels (a)–(c) of Fig. 7.6 show the bi-dimensional nNPS distributions for the clinical system and SR data with smooth and sharp PhR kernels. The noise in the clinical system is much coarser than in SR images as visible in the insets in the top-left corner of each panel. Given that, as expected, the bi-dimensional nNPSs have circular symmetry, their radial profiles were computed and plotted in panel (d). Peak frequencies largely differ when comparing the two systems, being 0.4 mm^{-1} for the clinical BCT, 0.9 mm^{-1} and 1.4 mm^{-1} for the synchrotron images reconstructed
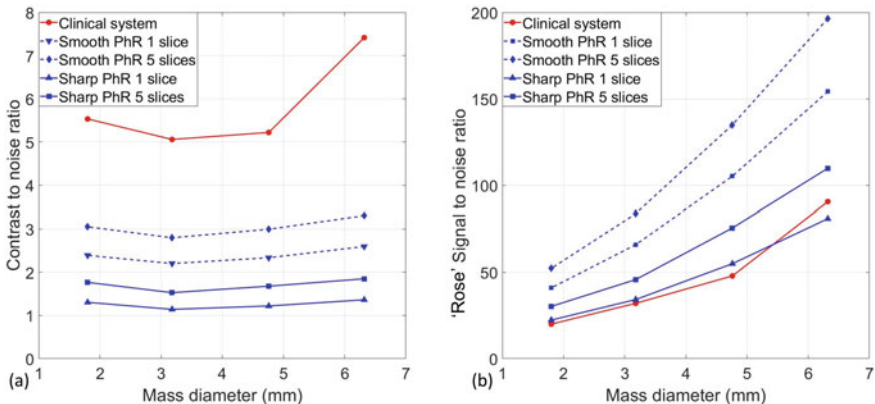
Fig. 7.5 CNR (**a**) and SNR_{Rose} (**b**) as a function of mass dimension for clinical the breast CT (red solid line) and SR breast CT with smooth (blue dashed lines) and sharp (blue solid lines) phase-retrieval kernels
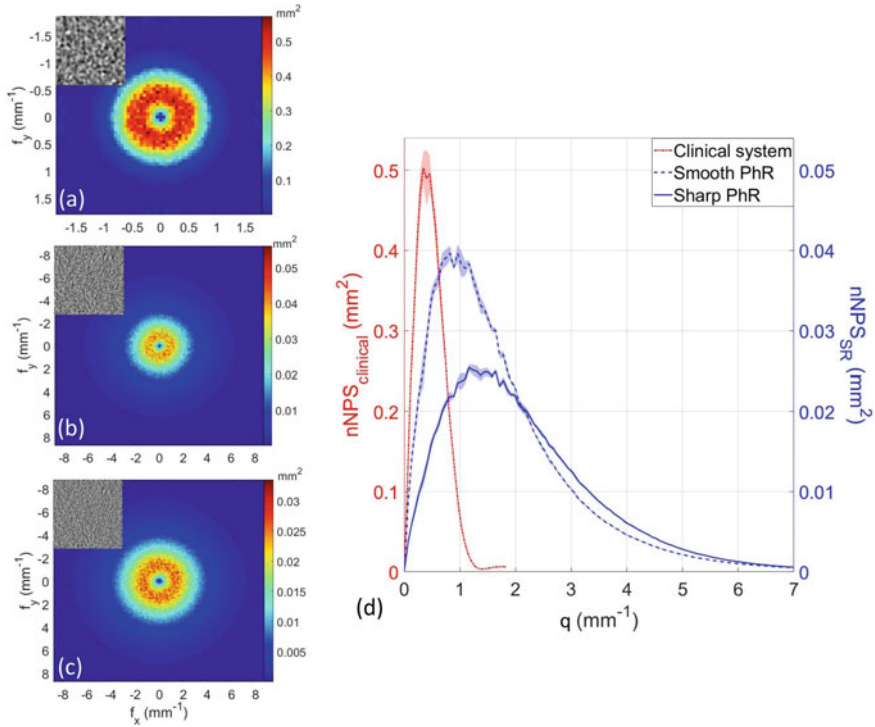
Fig. 7.6 Bi-dimensional nNPS for the clinical BCT system (**a**), synchrotron BCT with smooth (**b**) and sharp (**c**) PhR kernels. Of note, the extension of the frequency axis in (**a**) is different from (**b**) and (**c**). The inset in the top-left corner of each panel represents a 20×20 mm^2 homogeneous ROI. Radial averaged nNPS (**d**) for the clinical system (dashed red line) and SR BCT with smooth (dashed blue line) and sharp (solid blue line) phase-retrieval algorithm. Of note, the left y-axis refers to the nNPS of the clinical system while the right y-axis to the synchrotron data. The shaded region around each line represents one standard deviation uncertainty

with smooth and sharp PhR, respectively. In addition, the nNPS drops to 5% of its maximum value at 1 mm^{-1} for clinical BCT images, and at 5–6 mm^{-1} for SR datasets, meaning that the roll-off slopes of the nNPS curves are substantially different.

Following the procedure described in the previous section, the spatial resolution is estimated for all the different reconstructions as shown in Fig. 7.7: for each dataset a linear fitting region at small spatial frequencies is identified, where steeper linear fits indicate worse spatial resolutions. From the linear regressions the system resolutions were estimated to be 0.61 mm (FWHM) or 1.3 lp/mm (MTF$_{10\%}$) for the clinical BCT, 0.16 mm or 5.1 lp/mm for the smooth PhR and 0.12 mm or 6.8 lp/mm for the sharp PhR in SR images. The results of the quantitative analysis are summarized in Table 7.1.
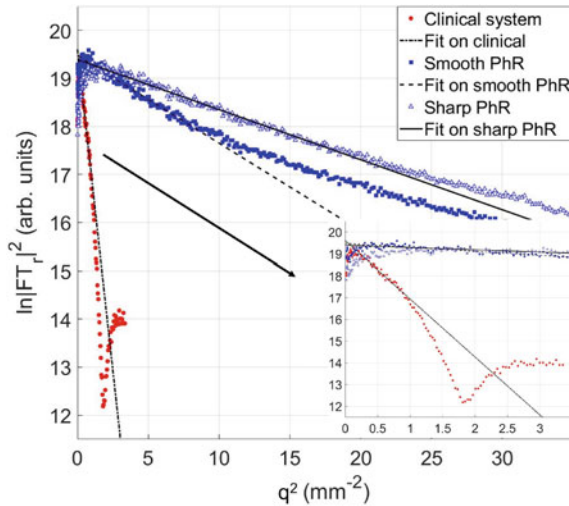
Fig. 7.7 Evaluation of the spatial resolution for the clinical system (red circles), and SR breast CT with smooth (blue squares) and sharp (blue-white triangles) PhR kernels. The logarithm of the absolute value of the radial Fourier transform is plotted as function of the square of the spatial frequency. The linear fit for each dataset is shown with black lines. The inset displays a zoom at lower spatial frequencies

Table 7.1 Summary of the quantitative analysis and comparison between the two systems: clinical BCT and SR datasets with smooth and sharp PhR kernels. For the sake of readability, the table reports the SNR_{Rose} and CNR values only for the 4.76 mm mass while, for the other masses, the quantitative values can be derived from Fig. 7.5. Where present, numbers enclosed within round brackets express the absolute uncertainty

	CNR	SNR_{Rose}	nNPS peak (1/mm)	FWHM (mm)	$MTF_{10\%}$ (lp/mm)
Clinical BCT	5.2	48	0.3	0.61 (0.02)	1.3 (<0.1)
Smooth PhR	2.3 (1 slice)	105	0.9	0.16 (<0.01)	5.1 (0.1)
	3.0 (5 slices)	135			
Sharp PhR	1.2 (1 slice)	55	1.4	0.12 (<0.01)	6.8 (0.1)
	1.7 (5 slices)	76			

Figure 7.8 displays the epoxy fibers for the clinical (a)–(d) and SR datasets with smooth (e)–(h) and sharp (i)–(l) PhR. All the fibers are visible in the SR breast CT regardless the PhR kernel, while the two smallest fibers (0.23 and 0.15 mm in diameter) are not distinguishable in clinical BCT images. Figure 7.9 shows image details of the calcification clusters for the clinical (a)–(d) and SR datasets with smooth (e)–(h) and sharp (i)–(l) PhR. For the clinical BCT system, no calcification cluster
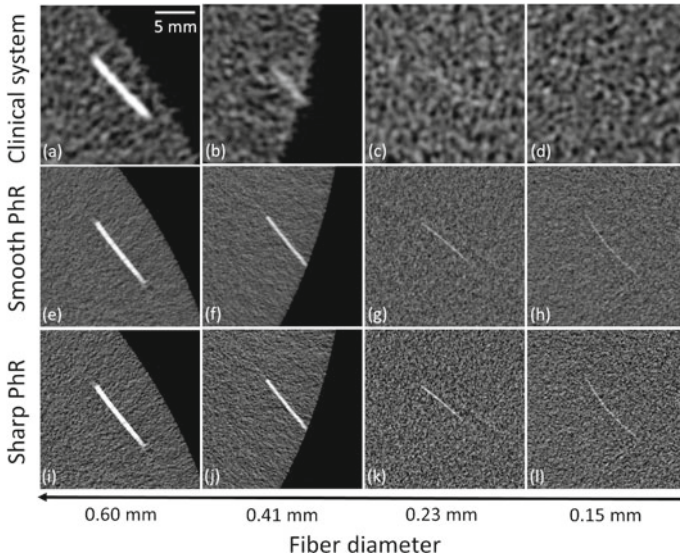
Fig. 7.8 Details of the epoxy fibers reconstructed (**a**)–(**d**) with the clinical BCT system, (**e**)–(**h**) smooth and (**i**)–(**l**) sharp PhR kernels for the SR BCT
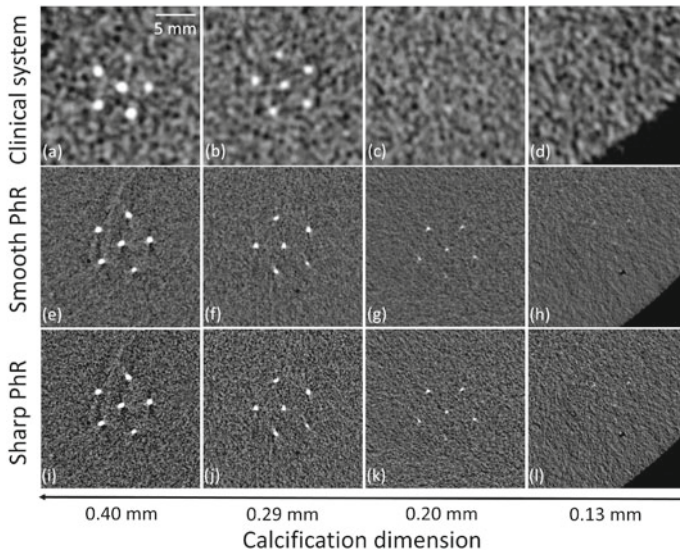
Fig. 7.9 Details of the calcification clusters reconstructed (**a**)–(**d**) with the clinical BCT system, (**e**)–(**h**) smooth and (**i**)–(**l**) sharp PhR kernels for the SR BCT

with diameter below 0.20 mm can be properly identified, while in the case of SR breast CT the smallest calcification (0.13 mm in diameter) represent the visibility limit for both the smooth and sharp PhR kernels.

7.1.4   BCT Image Quality Comparison: Discussion

From the data presented in the previous section it is clear that the gap in terms of image quality between clinical and SR breast CT systems is quite wide. The CNR in SR BCT images is found to be almost constant at different mass diameters, with small fluctuations mainly due to different noise levels. In particular, the two masses (dimensions of 3.18 and 4.76 mm) positioned closer to the center of the phantom show a slightly lower CNR with respect to the two located in the phantom's periphery: this behavior is compatible with the usual radial noise dependence observed in CT reconstructions (i.e. higher noise in the center, lower noise in the periphery). Coherently with results published in previous studies [18, 19], the smooth-kernel PhR yields a 2-fold higher SNR_{Rose} with respect to the sharp-kernel PhR. The SNR_{Rose} for the SR setup can be up to 3-times higher with respect to the clinical BCT if the smooth reconstruction kernel is used when the average of 5 slices is considered, or more than 2-times higher if no averaging is performed. This difference can be mainly attributed to the high-efficiency and low-noise of the photon-counting detector, to the presence of phase-contrast effects, and the subsequent application of phase-retrieval filter, and to the higher dose-efficiency of the synchrotron system due to the beam monochromaticity. In addition, thanks to the laminar shape of the beam and the large isocenter-to-detector distance, the SR setup allows to obtain inherently scatter-free images. Considering SR-based data, it should be noted that, if the noise of each slice was uncorrelated, the expected SNR_{Rose} and CNR increase due to the averaging of 5 slices would be of a factor $\sqrt{5}$, whereas the observed factor is much smaller (between 1.3 and 1.4). This is mainly related to the application of the phase-retrieval which, being a 2D filter in the projections domain, introduces a certain degree of correlation also between neighbouring pixels belonging to different rows of pixels, hence to different slices.

The nNPS evaluation revealed that the synchrotron images have a 3 to 5 times higher peak frequency (for the smooth and sharp PhR kernels, respectively) and a generally shallower roll-off slope, meaning that the contribution to the image noise is not negligible up to 6 mm^{-1}, to be compared with 1 mm^{-1} of the clinical system's case. In addition, it is worth noting that the NPS peak frequency for the clinical BCT, i.e. 0.4 mm^{-1}, is consistent with previous findings by Betancourt-Benitez and colleagues [7], who characterized the system before its commercialization. The observed differences in terms of nNPS between clinical and synchrotron data reveals that the SR setup imaging chain (i.e. detector, image processing and tomographic reconstruction) provides generally sharper or, equivalently, less correlated noise: this is ultimately related to the smaller detector pixel size and to the higher image-sharpness offered by direct-conversion photon-counting detectors.

Despite being a model containing several simplifications (e.g., the PSF is assumed to be constant and Gaussian throughout the image) not allowing a detailed description of the system PSF (e.g., resolutions in radial and tangential directions cannot be uncoupled), the spatial resolution assessment through images of the homogeneous phantom has been proven to a robust and easy-to-implement technique. In facts, the results obtained on the SR images, with both the smooth and sharp PhR kernels, are compatible with conventional spatial resolution estimates (based on the edge spread function technique) documented in Chap. 5 and in other studies [19–21]. Quantitatively, the spatial resolution of the SR system was found to be 4 to 5 times better than the clinical system (5–7 lp/mm for the synchrotron to be compared with 1.3 lp/mm for the clinical setup). Interestingly, synchrotron images outperform every clinical breast CT setup reported in literature so far in terms of spatial resolution, the maximum being 5 lp/mm for a photon-counting breast CT system proposed by Kalender and co-workers [22–24]. The qualitative analysis in terms of detail visibility showed that both the smallest fibers (i.e. diameter of 0.15 mm) and calcification clusters (i.e. diameter of 0.13 mm) can be detected in the SR-based images, while details with dimension in the order of 0.20 mm or below cannot be properly identified in the clinical BCT system. As mentioned in the previous chapter, the correct detection of such details plays a crucial role in the diagnostic process since both the presence of microcalcifications and spiculae (i.e. small fibers protruding from a bulk mass) are signs of malignancy.

Before concluding this section, it should be remarked that the implementation of SR BCT to the clinical realm presents also some practical drawbacks, the main being the longer scan time with respect to clinical systems due to the limited vertical dimension of the beam, to the need for patient rotation and to the limited detector readout speed. This can lead to motion artifacts due to both voluntary and involuntary movements of the patient, possibly impairing image quality (mainly spatial resolution). This issue has been encountered also in a clinical context suggesting the use of a breast immobilizer [25]. As mentioned in Chap. 6, the SYRMA-3D collaboration is devoting several efforts towards the reduction of the scan time, while the usefulness of immobilization systems is being investigated.

7.2 Monochromatic PB Micro-CT with a Rotating Anode Source

In the previous section a comparison between a synchrotron and a (conventional) clinical system was performed focusing on a specific imaging application, i.e. BCT. The two systems largely differ in terms of geometry, detector and, most importantly, X-ray quality, where the SR spatial and temporal coherence provide the key advantage over the clinical BCT. On the other hand, compact laboratory setups (as opposed to SR setups) based on conventional X-ray sources enabling monochromatic phase-contrast imaging exist, even if their application usually focuses on small samples (i.e. in the

millimeter scale) due to the limited field of view and/or limited flux. These limitations impose *a fortiori* a shift from clinical to preclinical or nonclinical studies, often based on *ex-vivo* samples. Nonetheless, the higher contrast or contrast sensitivity offered by phase-sensitive techniques when imaging soft samples, represents a key advantage over attenuation imaging.

In this section, a monochromatic PB micro-CT system based on a state-of-the-art rotating anode source is presented, reporting a detailed characterization, both in planar and tomographic configurations, and applications to two biological samples of medical interest. In addition, some practical considerations on possible trade-offs between scan time and image quality as well as improvements on the presented setup are discussed. All the experimental work hereby presented has been carried out at the X-ray Phase Contrast Imaging laboratory of the Department of Medical Physics and Biomedical Engineering of University College London (London, UK) and partly described in [26].

As discussed in Sect. 2.2, over the last two decades, many phase-sensitive techniques have been developed (e.g.., propagation-based, analyzer-based, edge-illumination, interferometric etc.) and most of them are in use with synchrotron and, in some cases, conventional sources [27–30]. As mentioned, propagation-based imaging is, in terms of experimental setup, the simplest to implement as in principle it does not require optical elements or multiple exposures. On the other hand, in terms of X-ray source characteristics, PB has more stringent requirements, demanding for high spatial coherence and, especially at small magnifications, high detector spatial resolution. For this reason, most of its applications have been so far limited either to synchrotron radiation facilities or to low-power micro-focal sources [28, 31–34]. In this context, the development of compact and partially coherent high-flux X-ray sources is an active area of research [35, 36].

Several laboratory X-ray sources, based either on liquid-metal, fixed or rotating targets, are capable of producing sufficient flux and spatial coherence to be used for phase-contrast imaging purposes, the main advantages over synchrotrons being availability, compactness and low costs [37–40]. Moreover, monochromator crystals selecting the characteristic X-ray lines can be coupled to the source, thus producing quasi-monochromatic spectra. It is noteworthy that, albeit not being essential for PB imaging, the use of narrow monochromatic radiation is advantageous even when no dose-efficiency constraints are present, as it allows performing a straightforward quantitative analysis and avoiding beam hardening effects.

In the following, the theoretical background presented in Chap. 2 will be widely used to characterize the system in terms of spatial resolution, coherence, quantitativeness, stability, and contrast sensitivity. Planar and tomographic images of custom-built wire phantoms are compared with theoretical predictions. In addition, the applications on two biological samples of medical interest demonstrate the feasibility of monochromatic PB imaging μ-CT with laboratory-compatible exposure times from tens of minutes to hours.

7.2.1   System Characterization

A schematic overview of the experimental setup is given in Fig. 7.10. X-rays are pro-
duced by a Rigaku Multi-Max 9 rotating anode source, featuring a copper anode and
operated at 46 kV(peak) and 26 mA corresponding to a power of 1.2 kW. The source
is coupled to a double bent multilayer VariMax Cu-HF monochromator, providing an
energy resolution of about 1% at 8 keV (copper k_α emission lines) and focusing the
beam to a 210 μm focal spot [41, 42]. The source dimension is defined by a golden
plated pinhole collimator with a diameter of 75 μm, located at the focus position of
the monochromator. This arrangement (i.e. monochromator and collimator) results
in an integrated flux of about 10^8 ph/s and a divergence of 5 mrad. The sample was
positioned at 88 cm from the source, while the propagation distance was set to 11 cm,
corresponding to a magnification of M = 1.13. At this distance, the field of view was
diamond shaped with dimensions of about 5×5 mm^2. The sample alignment and
rotation were performed through a piezometric motor stack with 5 degrees of freedom
and sub-micrometric precision. The imaging detector was a charge-coupled device
(CCD) camera featuring a 4.54 μm pixel size, coupled through a fiber-optic plate
to a Gadox scintillator (Photonic Science). Both the detector PSF and the source
intensity distribution were measured with the slanted edge technique by using a 50
μm thick lead blade, the unsharpness and finite-thickness effects of which can be
neglected given the system energy and spatial resolution [43]. The absorbing edge
was placed alternatively close (distance of 10 cm) to the source and in contact with the
detector to provide independent measurements of the source dimension and detector
PSF, respectively. As a cross-check, the blade was also positioned at sample position
yielding, by taking into account the magnification, consistent results.

The overall spatial resolution of the system is the key parameter in determining
whether or not phase effects can be observed. Therefore, the overall system PSF was
evaluated as:
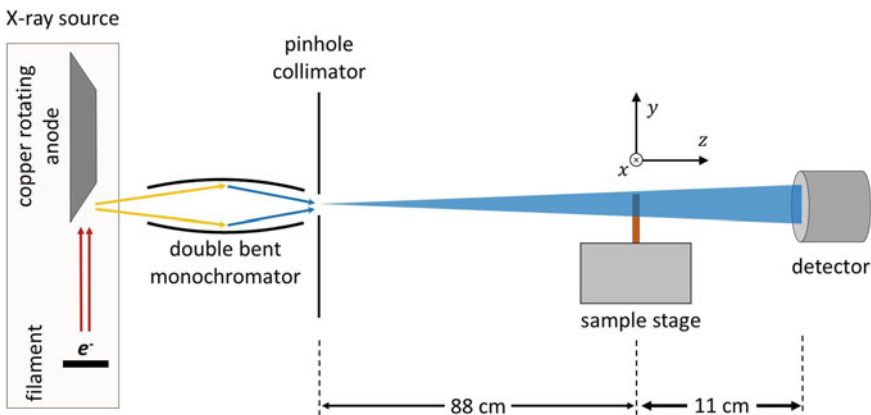
Fig. 7.10   Schematic overview of the experimental setup
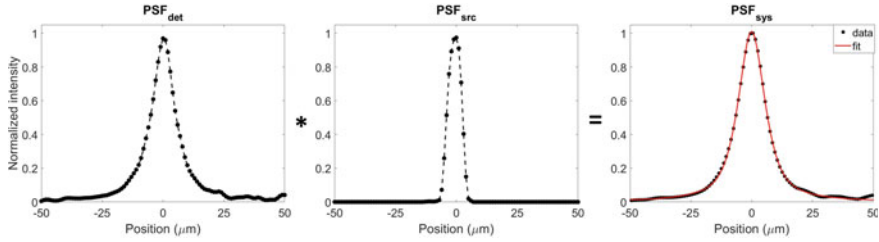
Fig. 7.11 Detector (left), source (center) and system (right) PSFs projected at the sample position. The system PSF has been fitted (red solid line) with a linear combination of Lorentzian and Gaussian functions

$$\mathrm{PSF}_{\mathrm{sys}}(x, y; M) = \mathrm{PSF}_{\mathrm{det}}(Mx, My) * \mathrm{PSF}_{\mathrm{src}}\left(\frac{M}{M-1}x, \frac{M}{M-1}y\right) \qquad (7.8)$$

where this expression is analogous to Eq. (2.13) computed at sample position instead of detector position. In Fig. 7.11 the measured detector PSF (left), source distribution (center), and their convolution (right) are reported as a function of the spatial coordinate at the sample position according to Eq. 7.8. The experimental system PSF has been fitted with a linear combination of a Lorentzian and a Gaussian function. The blurring due to the detector response is of 12 μm full-width-half-maximum (FWHM), while the source size projected at the sample position is of about 10 μm, resulting in an overall resolution of about 14 μm FWHM.

Given the system PSF, the intensity profile given by a wire of known composition can be theoretically calculated according to Eq. (2.8), where the refraction angle produced by a cylinder (i.e. wire) oriented along the y direction can be analytically expressed as:

$$\alpha(x) \simeq \frac{2\delta x}{\sqrt{r^2 - x^2}} \qquad (7.9)$$
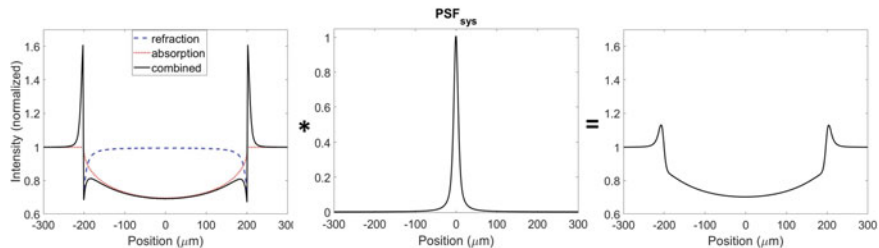
Fig. 7.12 Theoretical refraction, attenuation and total profiles produced by a homogeneous wire (left), system PSF (center), their convolution (right)

In the left panel of Fig. 7.12 the refraction (blue line), transmission (red line), and total (black line) intensity profiles calculated according to Eq. 2.12 are reported. Despite the smearing due to the convolution with the system PSF (central panel), the expected signal (right panel) still shows edge-enhancement contrast, indicating that the system spatial coherence and spatial resolution are sufficient to detect phase effects.

7.2.2   Acquisition Parameters and Data Processing

Two *ad-hoc* built wire phantoms have been imaged in planar and tomographic geometries, respectively. The planar acquisition was performed with an overall exposure time of 100 s whereas the long exposure CT-scan was acquired over 1440 projections with an exposure time of 10 s per projection, corresponding to a total exposure time of 4 hours. The tomographic scan has been repeated with a 20 times shorter exposure time (i.e. fast scan), acquiring 720 projections with an exposure of 1 s, resulting in a total exposure of 12 minutes. Similarly, in the long scans, the biological samples have been imaged with the same number of projections and an exposure time of 6 s per projection, corresponding to a total exposure of 2.4 hours, whereas the short scan has been obtained by reducing the exposure of a factor of 10, i.e. acquiring 720 projections of 1.2 s each, resulting in a total exposure of 14 minutes.

The planar data were processed by a conventional dark current subtraction and flat field normalization, whereas for CT scans the projections have been normalized using a dynamic flat field approach based on the principal component analysis of the flat images to compensate for beam intensity variations over long exposures [44]. The normalized projections have been (optionally) phase-retrieved and reconstructed through the same reconstruction software used to process synchrotron-based data [45], as detailed in Sect. 3.7. Of note, the reconstruction has been performed assuming a parallel beam geometry irradiation since, considering the small sample sizes and setup geometry, the beam divergence within the sample was smaller than the system spatial resolution, thus not requiring the use of a cone beam reconstruction.

7.2.3   Plastic Phantoms

Both the wire phantoms consisted of 3 different high-purity plastic rods made of Polybutylene terephthalate (PBT), Polyethylene terephthalate (PET), and Nylon. The real and imaginary parts of the refractive index used for the theoretical calculations are listed in a publicly available database [46] and are reported in Table 7.2.

The first test of the system quantitativeness was performed by imaging a planar phantom consisting of 3 vertically oriented wires made of PBT, PET and nylon, plus 1 horizontal PBT wire (panel (a) of Fig. 7.13). For each of the vertical wires, a line

Table 7.2 Physical properties of the wires used for the phantoms

	$\delta \times 10^{-6}$	$\beta \times 10^{-9}$	δ/β	Density (g/cm^3)	Diameter (μm)
PBT	4.45	9.79	454	1.31	180
PET	4.70	11.1	423	1.40	400
Nylon	3.99	7.25	550	1.13	160
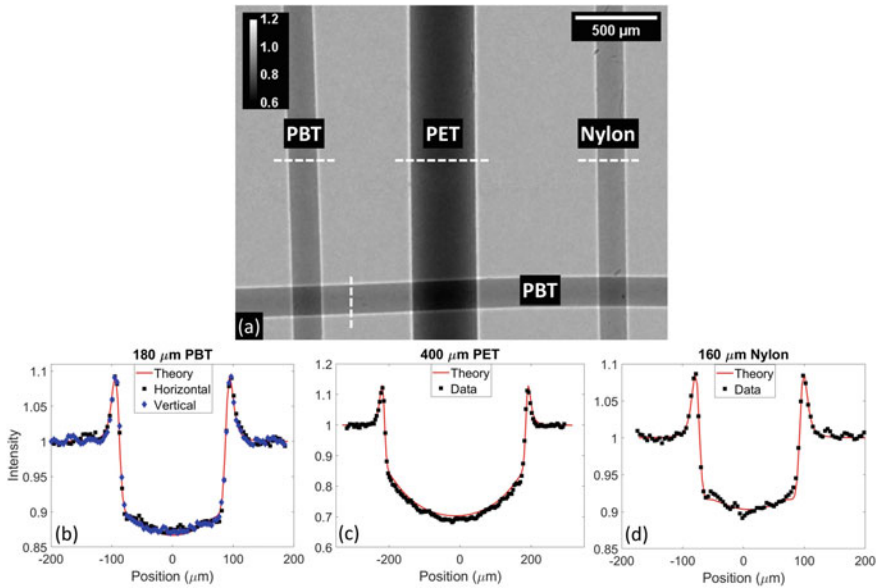
Fig. 7.13 Image of the planar wires phantom (**a**) and plots of the intensity profiles (**b**)–(**d**) along the white dashed lines. The image results from dark current subtraction and flat field normalization

intensity profile is compared against their respective theoretical profiles, accounting for the nominal values of density, attenuation and refraction of each material (b)–(d). The overall agreement between theory and experimental data is remarkable both considering phase and attenuation contrast, the largest discrepancy being a slight underestimate ($< 5\%$) of the PET attenuation. Moreover, by comparing profiles extracted from both the horizontal and vertical PBT wires (b), the same phase sensitivity is achieved in both directions due to the circular symmetry of the source.

Wires of same materials and sizes were used to assess the system performances in CT acquisitions. In panel (a) of Fig 7.14, a tomographic slice of the long scan is shown: thanks to the beam monochromaticity the reconstruction is inherently quantitative, thus, far from the sample boundaries where the edge-enhancement effect is present, the gray level represents the linear attenuation coefficient. To obtain the theoretical profiles for the CT case, a sinogram composed by a set of identical line profiles was created for each wire and then reconstructed following the same workflow used
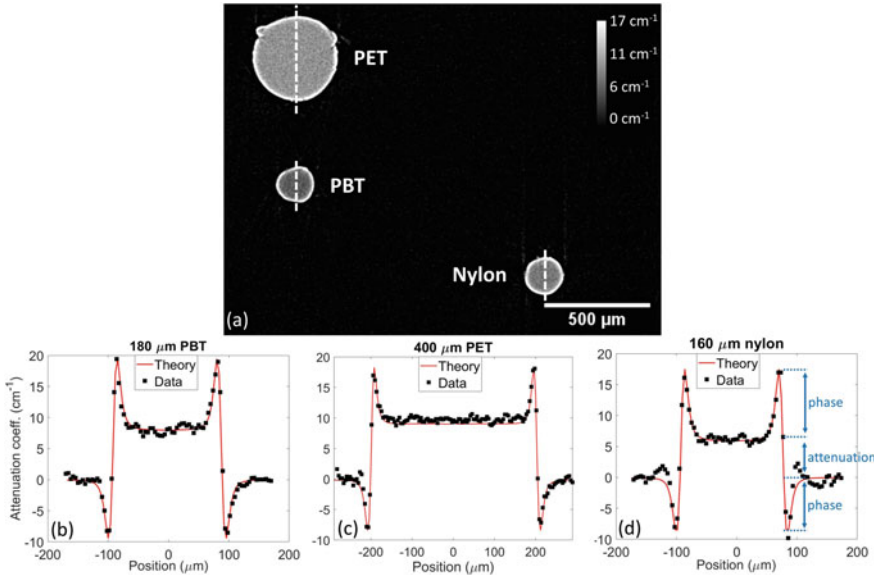
Fig. 7.14 Reconstructed slice of the wire phantoms (**a**) and plots of the intensity profiles (**b**)–(**d**) along the white dashed lines. The structure visible in the top corners of (**a**) is part of the cylinder that was used to keep the phantom in place

for the experimental data. As for the planar image, a good agreement is observed when comparing theoretical and experimental profiles across the wires for both phase and attenuation signals, except for a small discrepancy ($<10\%$) in the attenuation coefficient of PET (b)–(d). The fact that the refraction fringes (i.e. edge-enhancement signal) are well matched by the theoretical predictions for a scan acquired over several hours, provides an indirect assessment of the system stability and piezometric motors reproducibility: vibrations or spatial drifts of the source, sample or detector, or slight inaccuracies in the sample repositioning after the periodic flat field images acquisition, would result in a broader effective PSF, thus smearing out the fringes. Furthermore, by defining the refraction (or phase-contrast) signal as the sum of the overshoots of dark and bright fringes (see panel (d)), this is in all cases between 1.5 and 3 times higher than the attenuation signal.

As discussed in Sect. 2.4, CT projections were processed by applying the Paganin's single shot phase-retrieval algorithm. In order to adequately choose the filter parameter, it is common practice to tweak δ/β until refraction fringes disappear without introducing an excessive smoothing. Such a procedure is often applied when dealing with polychromatic X-ray spectra or with samples of unknown composition. To demonstrate this practice, several profiles taken across the PBT wire are shown in Fig. 7.15. Each profile has been reconstructed using a δ/β value in the range 250–550: thanks to the beam monochromaticity, it is found that the optimal δ/β is 450 that well matches its nominal value (see Table 7.2).

Fig. 7.15 Intensity profiles
across the PBT wire at
different δ/β values
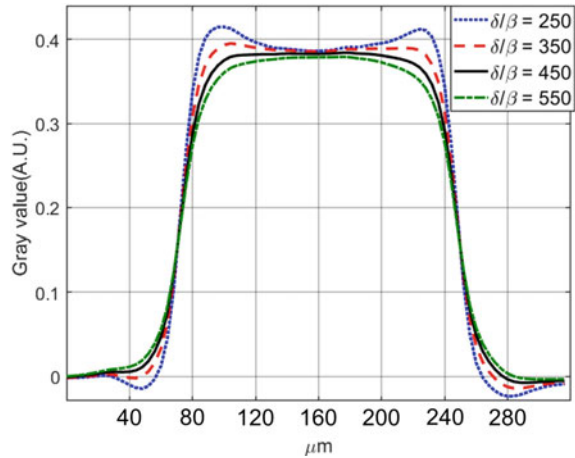
In Fig. 7.16, panel (a), the phase retrieved reconstruction of the wire phantom
is shown. Here a $\delta/\beta = 450$ is used, as it is an intermediate value among the three
different plastics. As expected, the refraction fringes are no longer visible, while
the noise has been significantly suppressed due to the 'low-pass filtering' effect of
phase-retrieval detailed in Sect. 5.1. This can be clearly appreciated in the gray level
histograms in panels (c), (d), which are obtained by selecting circular ROIs at the
center of each wire for both the images with and without the phase retrieval: after
phase retrieval the three materials can be easily separated based on the gray values of
each voxel. The ROIs are selected far from edges where the gray level distribution is
flat and have equal areas to provide histograms with equal statistics. Given the major
increase in contrast sensitivity achieved with the phase retrieval, it is interesting to
observe the results obtained from the same sample scanned with a 20-fold shorter
exposure time, as shown in panel (b). Even though a broadening of the distributions
due to the reduced statistics can be seen, the histogram in panel (e) shows that the
materials are still clearly distinguishable. In quantitative terms, we observe that the
central values of the gray level distributions are separated, respectively, by ∼25
standard deviations for the long and ∼10 for the short exposure scans. This clear
separation, between materials of similar attenuation properties, is advantageous in all
those applications involving subsequent data processing steps such as segmentation.

The quantitative results extracted from tomographic images are summarized in
Table 7.3. For all materials, the measured attenuation coefficient is compatible, within
the noise fluctuations, with the theoretical values; the maximum discrepancy in terms
of mean value is observed for PET wire and it is smaller than 10%. This result is
compatible with the findings of the planar image where PET has been found to be
more absorbing than its nominal value. To estimate the effects of phase retrieval, the
contrast with respect to the least absorbing material, i.e. Nylon, has been measured
both before and after the application of the retrieval algorithm. As expected, no
significant differences in the detected contrast are observed, indicating that the image
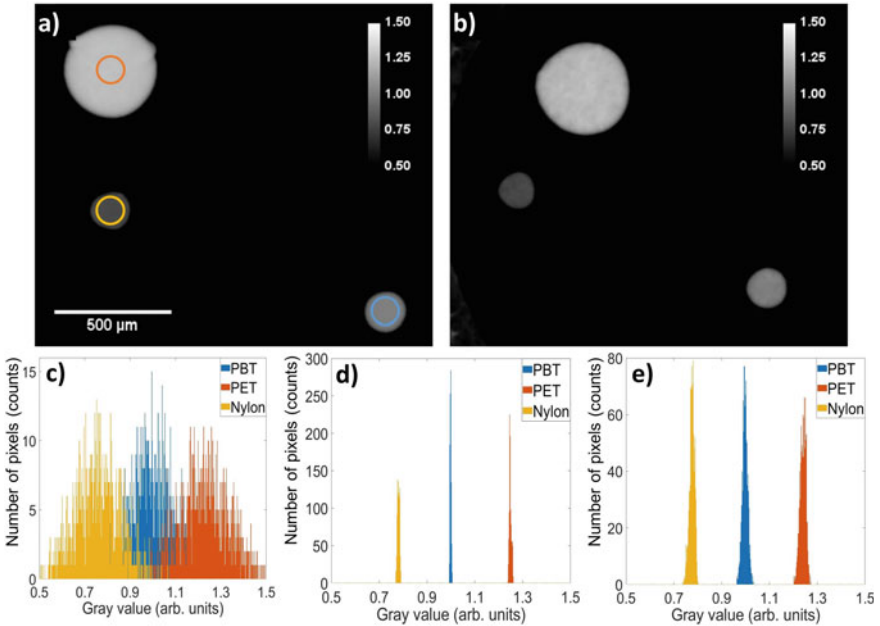
Fig. 7.16 Image of the wire phantom after phase retrieval for the 4 hours long exposure (**a**) and the 12 minutes long exposure (**b**). In (**a**) the ROIs used for the histograms are reported. Gray level histograms are relative to the wires phantom reconstructed without (**c**, see also Fig. 7.15) and with phase retrieval for the long (**d**) and short (**e**) exposures

Table 7.3 Quantitative results obtained from CT reconstructions. C–no phrt, C–phrt and C–phrt short refer to the contrast of long exposure non-phase-retrieved, phase-retrieved and short exposure phase-retrieved acquisitions, respectively, whereas subscript th and exp refers to theoretical and experimental values, respectively. Uncertainties are computed by following standard error propagation rules

	μ_{th} (cm^{-1})	μ_{exp} (cm^{-1})	rel error (%)	C–no phrt (%)	C–phrt (%)	C–phrt short (%)
PBT	7.98	7.8±0.8	−1.8	30±18	27.9±0.7	28.5±2.0
PET	9.01	9.8±0.8	8.7	62±20	59.9±0.8	59.9 ±2.2
Nylon	5.91	6.0±0.8	2.0	–	–	–

retains its quantitativeness (see Sect. 2.6). On the contrary, a major improvement in the contrast sensitivity (i.e. the associated uncertainty), going from about 20% to values smaller than 1%, is found. Also when the short exposure acquisition is considered, the contrast sensitivity is still around 2%, clearly sufficient for material differentiation, while no contrast variation is observed.

7.2.4   Biological Samples

The scans of two biological samples were acquired to assess the imaging potential of the experimental setup on complex objects. The first sample is an esophageal acellular matrix (ACM), derived from a piglet, provided by Institute of Child Health (ICH). The ACM was derived via an established decelluarization technique named detergent enzymatic treatment (DET) [47, 48]. Following the DET the sample was critical point dried using CO_2. The sample has an approximate size of $5 \times 5 \times 3$ mm^3. The second sample is a lobe (dimension approximately $3 \times 5 \times 3$ mm^3) of a dehydrated fibrotic murine lung generated from bleomycin-induced lung fibrosis model (sample collected 28 days post-bleomycin, 25IU) as described by [49]. For CT acquisitions all the samples were positioned within a thin plastic cylinder fixed on the rotation stage.

In Fig. 7.17(a), (b), the long (exposure time of 2.4 hours) CT scan of the piglet ACM is shown before and after applying the phase retrieval ($\delta/\beta = 100$), respectively, whereas in (c) the short (exposure time of 14 minutes) scan of the same sample is reported. Focusing on the detail shown in panels (d–f), it is clear that the high noise in the non-phase-retrieved image possibly hampers the ability to differentiate soft tissues while, when phase retrieval is applied, the contrast sensitivity is sufficient to distinguish the 4 layers composing the esophageal wall, namely mucosa,
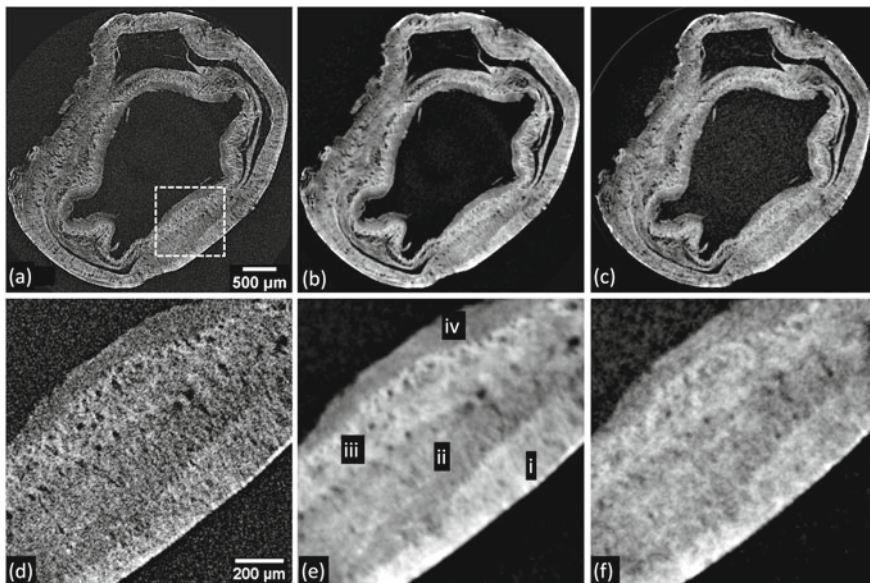
Fig. 7.17 Decellularized piglet esophagus scan with long exposure without (**a**), (**d**) and with (**b**), (**e**) phase retrieval, and short exposure with phase retrieval (**c**), (**f**). The dashed square in (**a**) represent the detail zoomed-in in the lower panels. The labels in (**e**) identify from right to left the adventitia (i), muscularis propria (ii), sub-mucosa (iii) and mucosa (iv)
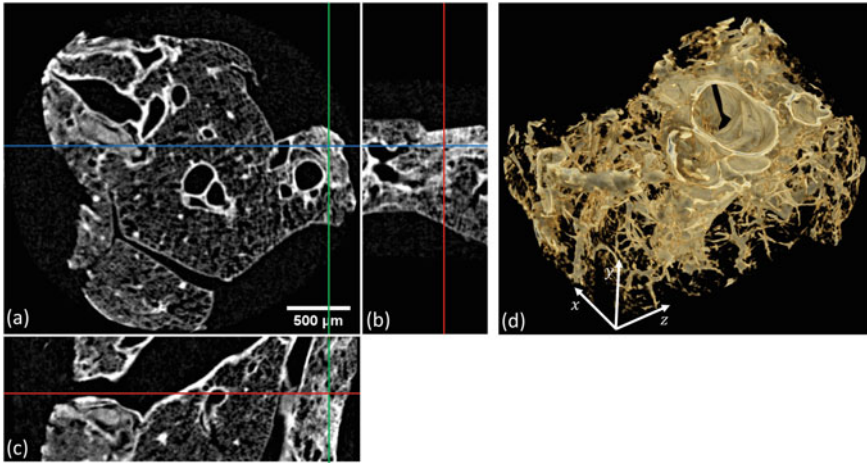
Fig. 7.18 Trans-axial (**a**), sagittal (**b**), transverse (**c**) slice and 3D rendering (**d**) of the fibrotic mouse lung sample

sub-mucosa, muscularis propria and adventitia. Remarkably, despite a higher noise level, the tissue layers are distinguishable also in the short exposure scan as visible in panel (e).

Panels (a)–(c) in Fig. 7.18 show the orthogonal views of the mouse lung sample phase-retrieved reconstruction ($\delta/\beta = 50$), while in panel (d) the 3D rendering is reported. Dense fibrotic tissue can be distinguished in the sub-pleural peripheral and bronchovascular regions, as shown for instance at the markers crossing position, with bronchi and bronchioles a prominent feature in the 3D rendering. Quantification of changes in parenchymal density, as seen in fibrosis, or measurement of airway or vascular remodelling represent potential pre-clinical applications of this imaging technique.

7.2.5   Remarks and Outlooks on High-Power Rotating Anode PB Systems

Most of laboratory phase-contrast imaging setups are based on polychromatic, low power, microfocal sources and cone beam scan geometries (i.e. large beam divergence) featuring high magnifications. Conversely, the results reported in this section show that quantitative PB imaging can be attained also by using compact high-power rotating anode sources which, coupled with dedicated optics, are capable of providing high-flux and temporal coherence. The geometry of this system resembles, in some way, the irradiation geometry commonly found in synchrotron facilities, where small magnifications and parallel beam reconstruction are used.

Specifically, the described setup can be appealing for light materials, such as plastics or soft tissues, with dimensions in the millimeter scale requiring high contrast sensitivity and spatial resolution in the order of 10 μm, while scan times range from hours to tens of minutes. The system, capable of delivering an integrated flux of 10^8 ph/s, has been characterized in terms of spatial coherence and detector spatial resolution, resulting in an overall PSF at the sample position of 14 μm FWHM: this value represents an optimal trade-off between spatial coherence and X-ray flux since the source size projected at the sample position is comparable to the detector PSF. The comparison between experimental data and theoretical prediction allowed to demonstrate the quantitativeness of the system, as an overall good agreement is found for both phase and attenuation signals, the maximum difference being $<5\%$ in planar and $<10\%$ in CT. In addition, the proposed setup has proven to be sufficiently stable over several hours, that was the time to acquire the high-statistics CT scans, while it is capable of providing a refraction (i.e. phase-contrast) signal 2–3 times higher than conventional X-ray attenuation. As done in the context of the synchrotron-based BCT project (see Chap. 5), the effects of the phase-retrieval algorithm on image noise and contrast sensitivity have been examined, showing that a 20-fold improvement in contrast sensitivity (from ∼20% to $\lesssim$1%) is achieved for the wire-phantom CT scan. This opens up the possibility of significantly reducing the exposure time: going from 4 hours to 12 minutes, contrast resolutions around 2% are found, still providing a fine resolving power between different soft materials. The tests on two biological samples of medical interest have shown the potential of the system in the field of pre-clinical applications as, for instance, digital histology or some aspects of regenerative medicine such as tissue/scaffold interactions, involving samples with dimensions in the millimeter scale.

As a general remark it is worth noting that, in addition to the configuration reported in this study, the setup is inherently flexible as it allows adjusting the spatial coherence, by replacing the pinhole collimator defining the source size, and the magnification. Moreover, by inserting a vacuum pipe to prevent air attenuation, the field of view can be in principle enlarged at a constant fluence rate. In fact, keeping the spatial coherence constant, the linear source size d (i.e. the collimator diameter) can be scaled with the source-to-detector distance $z_0 + z_1$, thus compensating the fluence rate reduction due to the larger source-to-detector distance by the larger dimension of the source:

$$\text{fluence rate}\left(\frac{\text{photons}}{\text{mm}^2 s^1}\right) \propto \frac{d^2}{(z_0 + z_1)^2} \propto \frac{(z_0 + z_1)^2}{(z_0 + z_1)^2} = \text{constant} \qquad (7.10)$$

This is possible since the focus created by the bent multilayer monochromator is significantly bigger ($\sim$210 μm) than the pinhole collimator itself (75 μm). Moreover, when using other X-ray phase-contrast techniques which are less demanding in terms of spatial coherence (e.g., edge illumination), the same setup can be used with larger collimators potentially delivering a 10 times higher flux.

Of course, despite providing remarkable performances for a such compact design, the integrated photon flux produced by the system presented in this section is more than 3 orders of magnitude smaller than the monochromatic flux achievable at the SYRMEP beamline, in an energy window one order of magnitude broader. In addition, while X-ray spectra produced in synchrotron rings by bending or wiggler magnets are broad, thus allowing a large flexibility in the energy selection, the monochromatic spectra extracted from conventional X-ray sources are limited to the choice of the anode material, therefore to its *k*-edges.

7.3 Do We Need Clinical Applications in Synchrotrons? A Tentative Answer

Going back to the initial question of this chapter, it is clear that synchrotron radiation facilities offer substantial advantages in X-ray imaging, as demonstrated for the breast CT case in Sect. 7.1, potentially being ideal sources also for clinical applications. On the other hand, a widespread diffusion of SR-based clinical exams is not feasible in terms of costs and infrastructural requirements. For this reason, the diffusion of many phase-contrast techniques, which have the potential to revolutionize X-ray diagnostic, is intrinsically linked to the development of 'synchrotron-like' radiation sources fitting a hospital environment. Therefore, any step forward in the translational research towards more compact sources should be encouraged by all means. In this context, machines based on the inverse Compton scattering [35, 50], which are able of providing sufficiently high coherence and X-ray flux at energies of radiological interest in a scale one or two orders of magnitude smaller than conventional synchrotron facilities, are envisaged as potential candidates to kick off the transition from synchrotrons to hospitals. Anyway, at present, sources of this kind with sufficient robustness and reliability are not available, and high spatial coherence or high output power are mutually exclusive properties of any commercial X-ray device. This dichotomy, ultimately related to the impossibility of dissipating huge heat loads as it would be required for small-focal spot high-power sources, has driven the research down to two separate roads. On one side, sources for medical applications, mainly based on the rotating-anode technology, have been developed pursuing high flux, to speed up the examination, optimized X-ray spectra/detectors, to increase contrast, and sophisticated voltage/current control strategies, to reduce or optimize radiation dose deposition. Typically, these sources have output powers in the order of several kilowatts but they do not feature high brilliance (i.e. number of photon per unit time, area and solid angle) due to the relatively large focal spot size. On the other hand, X-ray imaging laboratory sources, often based on thin transmission or liquid metal anodes, are usually optimized to achieve a small focal spot thus allowing for large geometrical magnifications and/or phase-contrast (mainly propagation-based) imaging. In general, these sources have a small output power in the order of watts but they usually have higher brilliance, the brightest being the ones featuring liquid metal

anodes which can tolerate heat loads exceeding the anode's melting point. Right in between these two approaches, several efforts are being dedicated to develop phase-contrast techniques which can be adapted to conventional medical imaging sources. This has been accomplished with some degree of success by using both Talbot-Lau interferometry [51, 52] and edge illumination [53, 54]. Both techniques make use of spatially-varying masks used to split the X-ray beam generated from a broad focal spot into multiple beamlets and to analyze the changes in phase or direction of each beamlet due to the presence of the sample. The presence of absorbing masks brings to a reduction of the X-ray flux, requires for a careful alignment (order of microns) and stability throughout the examination, and demands for a precise fabrication of the masks, which are often made of high-Z materials. The last two conditions are allegedly the most critical issues which, at present, have halted a wider diffusion of these techniques in the clinical context.

In general, synchrotron radiation offers an extremely valuable benchmark and SR-based experiments can provide gold-standards in terms of achievable image quality, defining, in practice, the upper-limit to the potential clinical development of any given technique. At the same time, it is the author's belief that only the successful application of SR-studies on human patients and the production of irrefutable results can trigger the medical community, attracting researchers and funds to make the developed techniques impactful and widely available. Additionally, techniques and technologies born and/or optimized at synchrotrons have not always been confined within large research facilities. As aforementioned, this is the case of phase-contrast techniques as grating interferometry and edge illumination which, firstly implemented at synchrotrons, have been translated to conventional sources. Similarly, propagation-based imaging of human-scale objects could be straightforwardly extended to more compact environments as soon as sources with adequate flux and coherence are available. Finally, it should be noted that the Elettra-based breast CT project described in this work is only one among the several ongoing or planned clinical projects in synchrotron facilities. As mentioned, the researchers of the Australian synchrotron (ANSTO) are developing their own breast CT clinical project [55], planning to start clinical examinations in two years time (2020/2021) and similar interests are also shared by the Indian synchrotron facility (Indus-2) [56]. Along with breast imaging, phase-contrast application to lung imaging has been attracting an increasing interest [57], and encouraging results on human-scale samples have recently appeared in the scientific literature [58]. Historically, besides phase-contrast imaging, one of the most widely investigated medical applications of synchrotron has been the K-edge subtraction technique applied to angiography and/or lung imaging. In this field many clinical systems have been developed over the years at various facilities world-wide as Stanford Synchrotron Radiation Laboratory (SSRL), National Synchrotron Light Source (NSLS), Haburger Synchrotronstrahlungslabor (HASYLAB), Photon Factory (PF), Budker Institute of Nuclear Physics and European Synchrotron Radiation Facility (ESRF) [59]. Moreover, in addition to imaging, clinically-oriented radiotherapy projects [60] are ongoing both at ESRF and ANSTO, while a similar activity is now kicking off at the German Synchrotron (DESY). Therefore, even if the ever-increasing number of synchrotrons is still rather small (around 60 worldwide), an

extensive use of these facilities for clinical applications has the potential to provide a relevant clinical impact.

References

1. Brombal L, Arfelli F, Delogu P, Donato S, Mettivier G, Michielsen K, Oliva P, Taibi A, Sechopoulos I, Longo R et al (2019a) Image quality comparison between a phase-contrast synchrotron radiation breast CT and a clinical breast CT: a phantom based study. Sci Rep 9(1):1–12. https://doi.org/10.1038/s41598-019-54131-z
2. Samei E, Krupinski EA (2018) The handbook of medical image perception and techniques. Cambridge University Press. https://doi.org/10.1017/9781108163781
3. O'Connell A, Conover DL, Zhang Y, Seifert P, Logan-Young W, Lin C-FL, Sahler L, Ning R (2010) Cone-beam CT for breast imaging: Radiation dose, breast coverage, and image quality. Am J Roentgenol 195(2):496–509. https://doi.org/10.2214/AJR.08.1017
4. Sechopoulos I, Feng SSJ, D'Orsi CJ (2010) Dosimetric characterization of a dedicated breast computed tomography clinical prototype. Med Phys 37(8):4110–4120. https://doi.org/10.1118/1.3457331
5. Ning R, Conover D, Yu Y, Zhang Y, Cai W, Betancourt-Benitez R, Lu X (2007) A novel cone beam breast CT scanner: system evaluation. In: International society for optics and photonics on medical imaging. Phys Med Imaging 6510:51030. https://doi.org/10.1117/12.710340
6. Benítez RB, Ning R, Conover D, Liu S (2009) NPS characterization and evaluation of a cone beam CT breast imaging system. J X-ray Sci Technol 17(1):17–40. https://doi.org/10.3233/XST-2009-0213
7. Betancourt-Benitez R, Ning R, Conover DL, Liu S (2009) Composite modulation transfer function evaluation of a cone beam computed tomography breast imaging system. Opt Eng 48(11):117002. https://doi.org/10.1117/1.3258348
8. Hernandez AM, Seibert JA, Nosratieh A, Boone JM (2017) Generation and analysis of clinically relevant breast imaging X-ray spectra. Med Phys 44(6):2148–2160. https://doi.org/10.1002/mp.12222
9. Beutel J, Kundel HL, Van Metter RL (2000) Handbook of medical imaging, vol 1. Spie Press. https://doi.org/10.1117/3.832716
10. Gureyev NYI, Timur E (2018) Image quality in attenuation-based and phase-contrast-based X-ray imaging. In: Russo P (ed) Handbook of X-ray imaging: physics and technology. Taylor and Francis, pp 275–305. ISBN 978-1-4987-4152-1. 10.1201/9781351228251
11. Verdun F, Racine D, Ott J, Tapiovaara M, Toroi P, Bochud F, Veldkamp W, Schegerer A, Bouwman R, Giron IH et al (2015) Image quality in CT: from physical measurements to model observers. Phys Med 31(8):823–843. https://doi.org/10.1016/j.ejmp.2015.08.007
12. Solomon JB, Christianson O, Samei E (2012) Quantitative comparison of noise texture across CT scanners from different manufacturers. Med Phys 39(10):6048–6055. https://doi.org/10.1118/1.4752209
13. Dolly S, Chen H-C, Anastasio M, Mutic S, Li H (2016) Practical considerations for noise power spectra estimation for clinical CT scanners. J Appl Clin Med Phys 17(3):392–407. https://doi.org/10.1120/jacmp.v17i3.5841
14. Mizutani R, Saiga R, Takekoshi S, Inomoto C, Nakamura N, Itokawa M, Arai M, Oshima K, Takeuchi A, Uesugi K et al (2016) A method for estimating spatial resolution of real image in the Fourier domain. J Micros 261(1):57–66. https://doi.org/10.1111/jmi.12315
15. Saiga R, Takeuchi A, Uesugi K, Terada Y, Suzuki Y, Mizutani R (2018) Method for estimating modulation transfer function from sample images. Micron 105:64–69. https://doi.org/10.1016/j.micron.2017.11.009
16. Yang K (2018) X-ray cone beam computed tomography. In: Russo P (ed) Handbook of X-ray imaging: physics and technology. Taylor and Francis, pp 713–747. ISBN 978-1-4987-4152-1. 10.1201/9781351228251

17. Bartels M (2013) Cone-beam X-ray phase contrast tomography of biological samples: optimization of contrast, resolution and field of view, vol 13. Universitätsverlag Göttingen. https://doi.org/10.17875/gup2013-92
18. Brombal L, Golosio B, Arfelli F, Bonazza D, Contillo A, Delogu P, Donato S, Mettivier G, Oliva P, Rigon L et al (2018c) Monochromatic breast computed tomography with synchrotron radiation: phase-contrast and phase-retrieved image comparison and full-volume reconstruction. J Med Imaging 6(3):031402. https://doi.org/10.1117/1.JMI.6.3.031402
19. Donato S, Brombal L, Tromba G, Longo R et al (2018) Phase-contrast breast-CT: optimization of experimental parameters and reconstruction algorithms. In: World congress on medical physics and biomedical engineering 2018. Springer, pp 109–115. https://doi.org/10.1007/978-981-10-9035-6_20
20. Brombal L, Donato S, Dreossi D, Arfelli F, Bonazza D, Contillo A, Delogu P, Di Trapani V, Golosio B, Mettivier, G et al (2018b) Phase-contrast breast CT: the effect of propagation distance. Phys Med Biol 63(24):24NT03. https://doi.org/10.1088/1361-6560/aaf2e1
21. Brun F, Brombal L, Di Trapani V, Delogu P, Donato S, Dreossi D, Rigon L, Longo R (2019a) Post-reconstruction 3D single-distance phase retrieval for multi-stage phase-contrast tomography with photon-counting detectors. J Synchrotron Radiat 26(2). https://doi.org/10.1107/S1600577519000237
22. Kalender WA, Kolditz D, Steiding C, Ruth V, Lück F, Rößler A-C, Wenkel E (2017) Technical feasibility proof for high-resolution low-dose photon-counting CT of the breast. Eur Radiol 27(3):1081–1086. https://doi.org/10.1007/s00330-016-4459-3
23. Sarno A, Mettivier G, Russo P (2015) Dedicated breast computed tomography: basic aspects. Med Phys 42(6Part1):2786–2804. https://doi.org/10.1118/1.4919441
24. Kalender WA, Beister M, Boone JM, Kolditz D, Vollmar SV, Weigel MC (2012) High-resolution spiral CT of the breast at very low dose: concept and feasibility considerations. Eur Radiol 22(1):1–8. https://doi.org/10.1007/s00330-011-2169-4
25. Rößler A, Wenkel E, Althoff F, Kalender W (2015) The influence of patient positioning in breast CT on breast tissue coverage and patient comfort. Senologie-Zeitschrift für Mammadiagnostik und -therapie 12(02):96–103. https://doi.org/10.1055/s-0034-1385208
26. Brombal L, Kallon G, Jiang J, Savvidis S, De Coppi P, Urbani L, Forty E, Chambers R, Longo R, Olivo A et al (2019b) Monochromatic propagation-based phase-contrast microscale computed-tomography system with a rotating-anode source. Phys Rev Appl 11(3):034004. https://doi.org/10.1103/PhysRevApplied.11.034004
27. Wilkins S, Nesterets YI, Gureyev T, Mayo S, Pogany A, Stevenson A (2014) On the evolution and relative merits of hard X-ray phase-contrast imaging methods. Phil Trans R Soc A 372(2010):20130021. https://doi.org/10.1098/rsta.2013.0021
28. Olivo A, Castelli E (2014) X-ray phase contrast imaging: from synchrotrons to conventional sources. Rivista del nuovo cimento 37(9):467–508. https://doi.org/10.1393/ncr/i2014-10104-8
29. Rigon L (2014) X-ray imaging with coherent sources. In Brahme A (ed) Comprehensive biomedical physics, vol 2. Elsevier, 193–216. https://doi.org/10.1016/B978-0-444-53632-7.00209-4
30. Bravin A, Coan P, Suortti P (2012) X-ray phase-contrast imaging: from pre-clinical applications towards clinics. Phys Med Biol 58(1):R1. https://doi.org/10.1088/0031-9155/58/1/R1
31. Cosslett V, Nixon W (1951) X-ray shadow microscope. Nature 168(4262):24–25. https://doi.org/10.1038/168024a0
32. Mayo S, Davis T, Gureyev T, Miller P, Paganin D, Pogany A, Stevenson A, Wilkins S (2003) X-ray phase-contrast microscopy and microtomography. Opt Express 11(19):2289–2302. https://doi.org/10.3109/02841851.2010.504742
33. Fella C, Balles A, Zabler S, Hanke R, Tjeung R, Nguyen S, Pelliccia D (2015) Laboratory X-ray microscopy on high brilliance sources equipped with waveguides. J Appl Phys 118(3):034904. https://doi.org/10.1063/1.4927038
34. Sowa KM, Jany BR, Korecki P (2018) Multipoint-projection X-ray microscopy. Optica 5(5):577–582. https://doi.org/10.1364/OPTICA.5.000577

35. Gradl R, Dierolf M, Hehn L, Günther B, Yildirim AÖ, Gleich B, Achterhold K, Pfeiffer F, Morgan KS (2017) Propagation-based phase-contrast X-ray imaging at a compact light source. Sci Rep 7(1):4908. https://doi.org/10.1038/s41598-017-04739-w

36. Töpperwien M, Gradl R, Keppeler D, Vassholz M, Meyer A, Hessler R, Achterhold K, Gleich B, Dierolf M, Pfeiffer F et al (2018) Propagation-based phase-contrast X-ray tomography of cochlea using a compaCT synchrotron source. Sci Rep 8(1):4922. https://doi.org/10.1038/s41598-018-23144-5

37. Tuohimaa T, Otendal M, Hertz HM (2007) Phase-contrast X-ray imaging with a liquid-metal-jet-anode microfocus source. Appl Phys Lett 91(7):074104. https://doi.org/10.1063/1.2769760

38. Krenkel M, Töpperwien M, Dullin C, Alves F, Salditt T (2016) Propagation-based phase-contrast tomography for high-resolution lung imaging with laboratory sources. AIP Adv 6(3):035007. https://doi.org/10.1063/1.4943898

39. Vittoria FA, Endrizzi M, Kallon GK, Hagen CK, Iacoviello F, De Coppi P, Olivo A (2017) Multimodal phase-based X-ray microtomography with nonmicrofocal laboratory sources. Phys Rev Appl 8(6):064009. https://doi.org/10.1103/PhysRevApplied.8.064009

40. Kallon G, Diemoz P, Vittoria F, Basta D, Endrizzi M, Olivo A (2017) Comparing signal intensity and refraction sensitivity of double and single mask edge illumination lab-based X-ray phase contrast imaging set-ups. J Phys D Appl Phys 50(41):415401. https://doi.org/10.1088/1361-6463/aa8692

41. Shimizu K, Omote K (2008) Multilayer optics for X-ray analysis. Rigaku J 24(1)

42. Oberta P, Platonov Y, Flechsig U (2012) Investigation of multilayer X-ray optics for the 6 kev to 20 kev energy range. J Synchrotron Radiat 19(5):675–681. https://doi.org/10.1107/S0909049512032153

43. Samei E, Flynn MJ, Reimann DA (1998) A method for measuring the presampled MTF of digital radiographic systems using an edge test device. Med Phys 25(1):102–113. https://doi.org/10.1118/1.598165

44. Van Nieuwenhove V, De Beenhouwer J, De Carlo F, Mancini L, Marone F, Sijbers J (2015) Dynamic intensity normalization using eigen flat fields in X-ray imaging. Opt Express 23(21):27975–27989. https://doi.org/10.1364/OE.23.027975

45. Brun F, Pacilè S, Accardo A, Kourousias G, Dreossi D, Mancini L, Tromba G, Pugliese R (2015) Enhanced and flexible software tools for X-ray computed tomography at the italian synchrotron radiation facility elettra. Fundamenta Informaticae 141(2–3):233–243. https://doi.org/10.3233/FI-2015-1273

46. Henke BL (2018) CXRO X-ray interaction with matter. http://henke.lbl.gov/optical_constants

47. Totonelli G, Maghsoudlou P, Georgiades F, Garriboli M, Koshy K, Turmaine M, Ashworth M, Sebire NJ, Pierro A, Eaton S et al (2013) Detergent enzymatic treatment for the development of a natural acellular matrix for oesophageal regeneration. Pediatr Surg Int 29(1):87–95. https://doi.org/10.1007/s00383-012-3194-3

48. Hagen CK, Maghsoudlou P, Totonelli G, Diemoz PC, Endrizzi M, Rigon L, Menk R-H, Arfelli F, Dreossi D, Brun E et al (2015) High contrast microstructural visualization of natural acellular matrices by means of phase-based X-ray tomography. Sci Rep 5:18156. https://doi.org/10.1038/srep18156

49. Scotton CJ, Hayes B, Alexander R, Datta A, Forty EJ, Mercer PF, Blanchard A, Chambers RC (2013) Ex vivo μCT analysis of bleomycin-induced lung fibrosis for pre-clinical drug evaluation. Eur Respir J erj01824–2012. https://doi.org/10.1183/09031936.00182412

50. Eggl E, Dierolf M, Achterhold K, Jud C, Günther B, Braig E, Gleich B, Pfeiffer F (2016) The munich compaCT light source: initial performance measures. J Synchrotron Radiat 23(5):1137–1142. https://doi.org/10.1107/S160057751600967X

51. Pfeiffer F, Weitkamp T, Bunk O, David C (2006) Phase retrieval and differential phase-contrast imaging with low-brilliance X-ray sources. Nat Phys 2(4):258. https://doi.org/10.1038/nphys265

52. Arboleda C, Wang Z, Jefimovs K, Koehler T, Van Stevendaal U, Kuhn N, David B, Prevrhal S, Lång K, Forte S et al (2019) Towards clinical grating-interferometry mammography. Eur Radiol 1–7. https://doi.org/10.1007/s00330-019-06362-x

53. Endrizzi M, Diemoz PC, Millard TP, Louise Jones J, Speller RD, Robinson IK, Olivo A (2014) Hard X-ray dark-field imaging with incoherent sample illumination. Appl Phys Lett 104(2):024106. https://doi.org/10.1063/1.4861855
54. Havariyoun G, Vittoria FA, Hagen CK, Basta D, Kallon GK, Endrizzi M, Massimi L, Munro PR, Hawker S, Smit B et al (2019) A compaCT system for intraoperative specimen imaging based on edge illumination X-ray phase contrast. Phys Med Biol. https://doi.org/10.1088/1361-6560/ab4912
55. Gureyev T, Nesterets YI, Baran P, Taba S, Mayo S, Thompson D, Arhatari B, Mihocic A, Abbey B, Lockie D et al (2019) Propagation-based X-ray phase-contrast tomography of mastectomy samples using synchrotron radiation. Med Phys. https://doi.org/10.1002/mp.13842
56. Sharma R, Sharma S, Sarkar P, Singh B, Agrawal A, Datta D (2019) Phantom-based feasibility studies on phase-contrast mammography at indian synchrotron facility indus-2. J Med Phys 44(1):39. https://doi.org/10.4103/jmp.JMP_98_18
57. Kitchen MJ, Buckley GA, Gureyev TE, Wallace MJ, Andres-Thio N, Uesugi K, Yagi N, Hooper SB (2017) CT dose reduction factors in the thousands using X-ray phase contrast. Sci Rep 7(1):15953. https://doi.org/10.1038/s41598-017-16264-x
58. Wagner WL, Wuennemann F, Pacilé S, Albers J, Arfelli F, Dreossi D, Biederer J, Konietzke P, Stiller W, Wielpütz MO et al (2018) Towards synchrotron phase-contrast lung imaging in patients—a proof-of-concept study on porcine lungs in a human-scale chest phantom. J Synchrotron Radiat 25(6). https://doi.org/10.1107/S1600577518013401
59. Thomlinson W, Elleaume H, Porra L, Suortti P (2018) K-edge subtraction synchrotron X-ray imaging in bio-medical research. Phys Med 49:58–76. https://doi.org/10.1016/j.ejmp.2018.04.389
60. Grotzer M, Schültke E, Bräuer-Krisch E, Laissue J (2015) Microbeam radiation therapy: clinical perspectives. Phys Med 31(6):564–567. https://doi.org/10.1016/j.ejmp.2015.02.011